


A study on the effect of print parameters on the internal structural quality of 316 L samples printed via laser powder bed fusion: Experimental and algorithmic approach

Suresh Alaparathi^{1,2} | Sharath P. Subadra^{1,2}  | Roy Skaria^{1,2} | Eduard Mayer^{1,2} | Shahram Sheikhi^{1,2}

¹Institute of Materials Science and Joining Technology, University of Applied Science Hamburg, Hamburg, Germany

²Forschungs- und Transferzentrum 3i, Institute of Materials Science and Joining Technology, University of Applied Science Hamburg, Hamburg, Germany

Correspondence

Sharath P. Subadra, Institute of Materials Science and Joining Technology, University of Applied Science Hamburg, Berliner Tor 13, Hamburg D-20099, Germany

Email:

sharath.peethambaransubadra@haw-hamburg.de

Funding information

Deutsche Forschungsgemeinschaft, Grant/Award Number: 532170006; Zentrales Innovationsprogramm Mittelstand; Bundesministerium für Wirtschaft und Klimaschutz

Abstract

This work aims to establish a quality assurance methodology for additively manufactured (AM) samples, produced from laser powder bed fusion (LPBF) method. The method incorporates resonance frequency method (RFM), where reference samples from wrought 316 L will be used to establish a data-base with a set of reference frequencies. The data-base is enhanced further with simulated frequencies, via FEM method, which was carried out on samples with the same dimensions and material properties as those of the reference. The quality of LPBF samples were benchmarked against this database. Four sets of LPBF samples (termed as A, B, C, and D) were printed with different parameters, and their densities were measured to understand deviations from the reference database. It was observed that Set-C had the least drop in density of approx. 0.65% when compared to the wrought samples. Microscopic analysis revealed that the melt pools were clearly visible in all the samples, with no significant effect from different print parameters. Subsequently RFM was performed on all the sets and clear shifts in frequencies observed. Set-C had the least deviation when compared to the reference (averaged at 200 Hz), whereas it was 250, 300, and 400 Hz for Set-D, Set-A and Set-B respectively. There are several reasons for the frequency shift, the presence of porosity being one of them. Set-B had the highest concentration of porosity in the -YZ plane. An algorithm was developed to sort the samples based on the frequency shifts seen from those of the samples from wrought 316 L. The sorting methodology was based on the shift frequencies, and the farther the sift is from the wrought the worst it get in terms of quality. The algorithm, which is programmed based on this methodology, was tested on a new set of LPBF samples and its effectiveness validated.

KEYWORDS

acoustics, additive manufacturing, algorithms, defects, laser powder bed fusion method, microstructure, non-destructive testing, porosity

This is an open access article under the terms of the [Creative Commons Attribution](https://creativecommons.org/licenses/by/4.0/) License, which permits use, distribution and reproduction in any medium, provided the original work is properly cited.

© 2024 The Author(s). *Engineering Reports* published by John Wiley & Sons Ltd.

1 | INTRODUCTION

Additive Manufacturing (AM) has gained increased prominence in several industrial sectors due to its ability to enhance functionality, productivity, and competitiveness. This potential enables the production of complex geometries that were previously challenging using conventional methods. Also known as three-dimensional (3D) printing, AM involves the layer-by-layer printing of materials from a 3D CAD model to create parts, distinguishing it from subtractive manufacturing approaches. Its applications extend across various industries, including aviation, automotive, healthcare, marine, oil and gas, and power generation.¹⁻⁴

Laser Powder Bed Fusion (LPBF) also known as Selective Laser Melting (SLM) stands as a crucial method in metal additive manufacturing. This technique employs a high-energy laser beam to fully melt the metal powder, followed by a cooling and solidification process, resulting in the production of intricately detailed, densely formed metal components with high precision.⁵ The ultimate outcome of products produced through LPBF relies on the careful choice of process parameters, including laser power, scanning speed, layer thickness, beam diameter, print strategy and Hatch distance, and so forth.⁶ E. Liverani⁷ investigated microstructure, defect formation and mechanical properties of AISI 316 L components by varying laser power from 100 to 150 W, hatch space from 0.05 to 0.07 mm and orientation from 45° to 90° and found that the laser power has the strongest influence on density, with highest relative density obtained at the highest investigated power level (150 W), while hatch spacing and building orientation do not induce significant effects over the tested range. Laser-related parameters involve laser power, spot size, wavelength, and the type of laser used. Scan-related aspects encompass scan speed, scan strategy, and hatch spacing. Powder-related considerations include layer thickness, size, bed density, material properties, and morphology. Temperature-related factors consist of powder feeder temperature, temperature uniformity, and powder bed temperature.⁸⁻¹⁰ It primarily impacts porosity, residual stress, fatigue, surface roughness, density, mechanical characteristics, and product microstructure.

Austenitic steel is a pivotal structural material known for its superior mechanical properties and resistance to pitting corrosion as well as its weldability. This low carbon-chromium-nickel-molybdenum alloy, which is used in nuclear power and aviation, outperforms conventional nickel-chromium stainless steels. Higher creep resistance, excellent formability, and reliable rupture and tensile strength at elevated temperatures are among its key characteristics. These features confirm its widespread use in a variety of engineering applications.⁹⁻¹¹ It has also been adopted in the LPBF technique due to its excellent weldability and is used in high value-added scenarios such as medical and dental applications, heat exchangers and so forth.¹² Gorsse et al.¹³ discovered that dense LPBF 316 L showed twice the yield strength of wrought 316 L while retaining adequate ductility. This is related to the cellular sub-structures found in LPBF 316 L, which have extraordinarily high dislocation density. The high density of dislocations is caused by fast solidification during LPBF.¹⁴ The final quality of products additively manufactured from 316 L depends on various parameters such print related parameters, microstructural features, mechanical properties and so forth¹² and hence should be taken care off.

As AM techniques lend itself to manufacture complex shaped parts, respecting quality standards are vital and difficult when dealing with complex geometries. This is true when dealing with geometries, which include elements that are inaccessible and cannot be verified by traditional metrology methods. Deep faults arising from uneven solidification and other process related parameters pose significant challenge in terms of quality, this along with complicated shapes make Non-Destructive Testing (NDT) an excellent tool to raise the caliber of AM products.¹⁵ NDT encompasses a set of techniques designed to identify both external (surface) and internal flaws within a structure. It has been in use for ascertaining the performance and quality of products and has been used widely in the industry and academia. Over the years, different methods have been developed¹⁶ to understand the presence of defects in materials. A few of the methods are visual inspection, dye penetrant method, magnetic powder method, eddy current method, thermography, acoustics and so forth. Despite the numerous advantages, non-destructive testing methods also face limitations, such as the economic factor associated with acquiring testing equipment.¹⁷

The resonant frequency method has been in use for several years and is based on the resonant response of materials and the components made of those materials. The test object is actively mechanically excited (either by impact or sweep excitation) in order to excite the resonance frequencies. The vibration response is then recorded (either by contact sensor or microphone). By using an appropriate algorithm, which will separate good and bad samples based on sound characteristics in addition to carrying out the filtering and transformation operations previously discussed.¹⁸ Therefore, owing to its versatility RFM as a quick NDT screening method for LPBF samples is worked upon in this paper. Carrying out comparisons with a reference sample frequency has been a vital technique used to understand the state-of-the-art on RFM technology to classify flawed samples, where a divergence from the reference sample frequency seen on another sample is interpreted as a defect on the component being examined, a broad review on this can be found in Reference 19. Therefore,

in our study we intend to precision mill a set of reference samples from wrought 316 L steel. The resonant frequencies of these samples would be recorded and used as a reference to check deviations of AM samples and class them based on quality.

Resonant frequencies obtained by FEM was used by Lee et al.²⁰ and Kam et al.²¹ to point out the defect position and the extend of it in a one-dimensional beam model. In the studies by References 22,23 used the modal analysis to evaluate the properties and integrity of metal additive manufactured parts and to detect defects in metal parts produced by SLM by fingerprinting method. In another study it was found that, the simulated and experimental frequencies coincided when an attempt was made to determine the viability of RFM identifying cracks in silicon wafers. But significant deviations were observed when broken wafer were considered, and this was explained due to interaction between the cracks.^{24,25} Therefore, based on this inference, the current study would try to re-evaluate if there is a congruence between the frequency of reference sample, and this information would be eventually used to build the algorithm which can classify SLM samples for their quality. This is to ensure that, the frequencies obtained via RFM has congruence with simulated frequencies, which in turn shall happen only if the correct material properties are used to simulate them.

The paper forms a part of a broad project funded by the Federal Ministry for Economic Affairs and Climate Protection (Germany) for developing innovative programmes/solutions for small and medium-sized enterprises. The end goal of the project is to develop a tool incorporating acoustic means to qualify LPBF samples, where the equipment is embedded with an algorithm, which enables sorting. Such equipment's should be cost effective and efficient to inform the user on the state of the quality of part printed via LPBF method. Though initially the equipment shall be constricted to simple geometries, the algorithm embedded in the system hardware can be easily modified to learn from data being fed into. This means machine learning techniques (supervised or un-supervised techniques) can be used and hence its robustness can be improved. The methodology adopted to sort the samples (also used by the algorithm) is based on a comparison with a reference that is not printed but precision milled from wrought 316 L material. To obtain repeatability 10 reference samples where milled and their resonance frequencies obtained, this was cross-checked with simulated results. A deviation from these resonance frequencies seen on LPBF samples having the same dimensions as the reference can only infer structural quality issues arising from the print parameters adopted to print such samples. Such a methodology to classify LPBF samples hasn't been used to the knowledge of the authors.

2 | METHODS

2.1 | Sample preparation from LPBF method

In this paper, four sets each with different parameters of LPBF samples were manufactured from 316 L steel powder. The chemical composition of 316 L is depicted in Table 1. A Renishaw AM 250 system was used to print LPBF samples perpendicular to the base plate, on which samples are printed. The Renishaw AM250 (Figure 1) is a 3D printer developed by Renishaw plc (Wotton-under-Edge, England, UK). It has a Maximum Laser Power of 200 W and build volume of 250 × 250 × 300 mm.

The chamber in Renishaw was filled with argon during the built time of the samples. Each set with varying parameters of the samples are assigned a code for the sake of convenience termed as A, B, C, and D. Here, Set A has the standard parameter and assumed to be the good samples vis-à-vis B, C, and D.

Each of the sample sets were built by a varying set of parameters namely laser power, hatch distance and layer thickness. These set of parameters were used to calculate the volumetric laser energy density, which defines the sample characteristics (e.g., flaws) to a larger extend. The equation 1 governing these parameters is elaborated below²⁶;

$$Ev = \frac{LP}{(HD * LT * SS)} \quad (1)$$

TABLE 1 Chemical composition of LPBF 316 L steel (wt.%).

Cr	Ni	Mo	Mn	Si	C	N	Nb	P	Fe
16.77	11.98	2.27	0.90	0.55	0.015	0.070	0.011	0.009	67.11

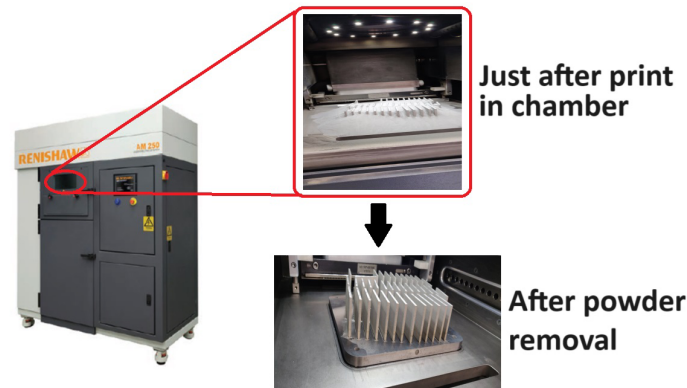


FIGURE 1 A typical Renishaw printer with samples seen on print plate post-print.

TABLE 2 Additive manufacturing process parameters.

Parameters	Set-A (Standard)	Set-B	Set-C	Set-D
Laser Power [W]	180	200	180	180
Scan Strategy	Stripe	Stripe	Stripe	Stripe
Hatch distance [mm]	0.08	0.08	0.1	0.08
Layer thickness [μm]	40	40	40	60
Scanning speed [mm/sec]	722	722	722	722
Volumetric laser energy density [J/mm^3]	77.90	86.56	62.32	51.93

where, LP is the Laser power [W], HD is the Hatch Distance [mm], LT is the Layer Thickness [μm] and SS is the scan speed [mm/sec] respectively. The parameters presented in Table 2 were chosen based on their critical impact on the LPBF process and the resultant properties of the 316 L stainless steel components. Laser power settings of 180 and 200 W were selected to understand the effect of different energy inputs on melt pool dynamics and microstructure, with higher power potentially increasing part density and mechanical properties. A consistent stripe scan strategy was used to control thermal gradients and minimize residual stresses. Hatch distances of 0.08 and 0.1 mm were examined for their effect on overlap between laser passes, with smaller distances potentially increasing density and larger distances reducing build time but risking increased porosity. Layer thicknesses of 40 and 60 μm were tested to assess their impact on resolution and build speed, with thinner layers expected to produce finer details at the cost of longer build times. The scanning speed was kept constant at 722 mm/sec to isolate the effects of other variables, chosen for its suitability in preliminary experiments. The derived parameter, volumetric laser energy density, ranging from 51.93 to 86.56 J/mm^3 , provided a comprehensive measure of energy input per unit volume, exploring a spectrum of densities to study their impact on part quality. These parameter variations are designed to systematically investigate the relationship between processing conditions and the quality of LPBF-manufactured 316 L stainless steel components, with the goal of optimizing parameters for the best combination of mechanical properties, density, and surface finish.

The steps involved in printing the samples are shown in Figure 2. The entire process can be divided into three stages. In stage-1, the sample was modeled on CAD software, and later it was sliced for the print file (shown in Figure 2A). In stage 2, the print was carried out, the chamber was cleaned, and the print plate removed along with the samples on it (see Figure 2B).

After termination of print, samples were removed from the base plate (stage-3). For RFM, printed samples have to be machined to guarantee the same geometry, which is necessary for frequency re-reproducibility. Table 3, shows the dimensions of all the LPBF samples after machining with a tolerance of ± 0.05 mm, this tolerance might affect the shift in resonant frequency, which is very small therefore, it is neglected for all the samples. For later calculations, the actual dimension of each sample was used to understand the deviations of frequencies. A set of 10 samples each were considered in the case of reference, Sets-A, -B, -C, and -D. Therefore, a total of 50 samples, to ensure that there is a credible database of frequencies for future references.

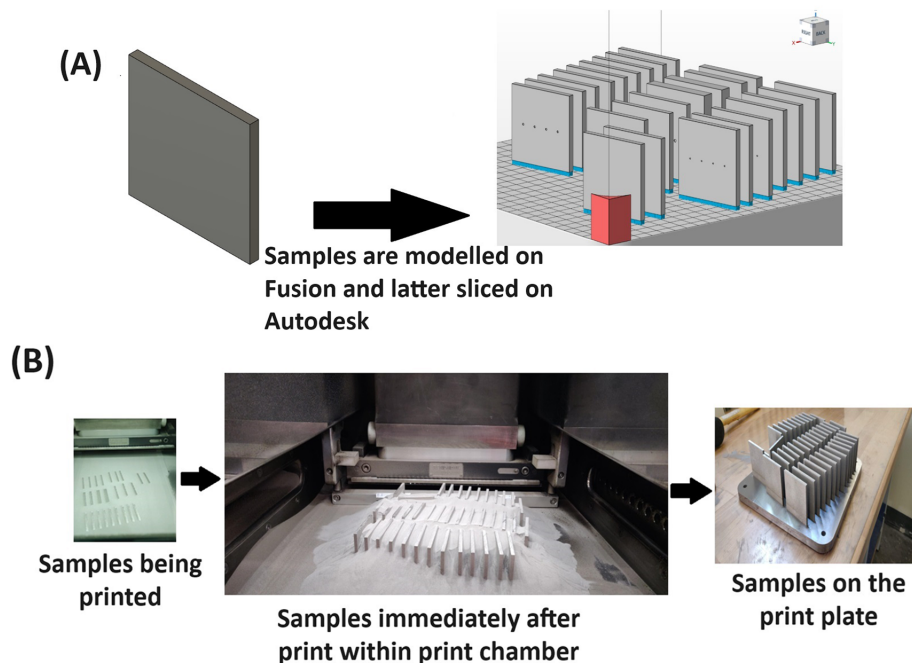


FIGURE 2 A typical print methodology, (A) Stage-1 and (B) Stage-2.

TABLE 3 Final dimension of the sample.

	wrought	Set A	Set B	Set C	Set D
Length, [mm]	50.15	50.15	50.15	50.15	50.15
Breadth, [mm]	50.09	50.05	50.05	50.05	50.05
Thickness, [mm]	4	4	4	4	4

2.2 | Density measurements

Density measurements were performed via metallographic method and according to the methodology established in ASTM B962 standard. Metallographic method involved evaluating the sample density for a specific plane in the micro-section, providing insights into localized variations. In contrast, the latter method offered an integrated density assessment for the entire sample volume. Further elaborating on this methodology, theoretical density of 316 L stainless steel is 7.99 g/cm^3 ,²⁷ utilizing Equation 2:

$$\text{Density} = \frac{Ma}{Ma - Mw} (dw) \quad (2)$$

where Ma represents the mass in air, Mw is the mass in water, and dw is the density of water, the density of each sample was determined. In the metallographic analysis, the samples underwent a series of preparation steps.

2.3 | FEM method for data-base enhancement

The resonant frequencies were ascertained through FEM simulations. Quadratic 3D elements were used for generation of mesh in the simulated parts, the mesh size was kept constant at 1 mm. Such a mesh size was arrived after conducting a parametric study of different mesh to precisely capture the resonant frequencies.²⁸ The samples were assumed as in free state condition in experimental, so no Boundary conditions are given in modal analysis as well. Material properties highlighted in Table 4 were adopted for wrought 316 L material, and the tests were performed as per ISO 6892, at Werkstoffprüfung Kunze GmbH (Hagen, Germany).

TABLE 4 Material properties of the samples considered.

Density [Kg/m ³]	E-modulus [GPa]	Poisson's ratio	Rp0.2 [MPa]	Rm [MPa]
7990	190	0.27	315	584

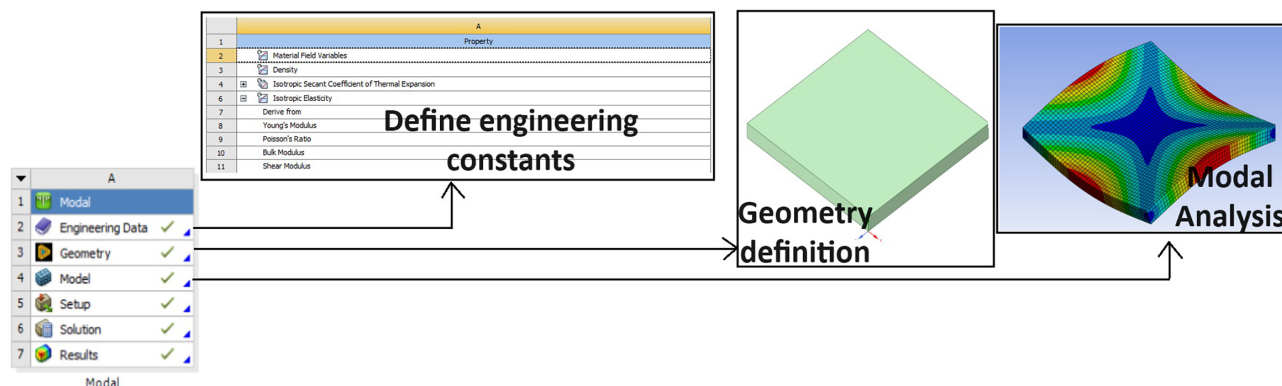


FIGURE 3 FEM modeling route on Ansys Workbench.

Initially, the samples were designed on CAD software and imported as STEP files into the geometry section of the modal analysis module of an FEM software, the individual sample dimensions were used. The material parameters elaborated in Table 4 where input in the engineering section of the module. The simulation route adopted is shown in Figure 3.

The FEM study serves two purposes in this study, first it helps in having a credible dataset of frequencies for the algorithm to be trained. Second, it assists in identifying frequencies associated with irrelevant modes, which are not necessary in this study. A parametric study would be carried out with varying E-modulus values and a fixed geometry. Thus, it enables to identify the correct frequencies, which are in proximity as those seen while conducting experiments.²⁹

2.4 | Resonant frequency measurement

To find the resonant frequencies, a variety of devices can be constructed; these are detailed in ISO EN 843.³⁰ While the resonant frequencies can be found, this standard is meant to determine the E-modulus of materials. This approach has a simple methodology: samples with similar geometry and material composition will have similar frequency spectra, and slight change in the sample's geometry or material composition will result in a change in the spectra. Peak frequency shifts can be used to observe this, and a statistical analysis on multiple samples can assist in accurately validating this shift. As a result, this technique is helpful for tracking structural alterations in any component. The number of samples affects this method's validity; the more samples used, the better the outcomes.^{31–34}

The setup for the experimental process is depicted in the figure below (Figure 4). The microphone is positioned along the middle axis, sometimes known as the anti-node, and the test piece (wrought 316 L) is suspended on threads around the periphery, slightly away from the vibration nodes. As the sample to be placed on fine plastic threads, hence the samples doesn't contain any Boundary conditions and can be assumed as free state condition. A different method was created to execute the Fast Fourier Transform in order to estimate the dominant frequency from the generated sound signal, which results in the generation of a power spectrum. The detected sound is transduced to an electric signal, which is then amplified. Based on a predetermined frequency range that it computes on its own using the sample dimensions and mechanical qualities referenced from literature (a database containing all Youngs modulus values), the algorithm is able to identify the necessary resonant frequencies from the spectrum. The next sections will provide a detailed explanation of the algorithm.

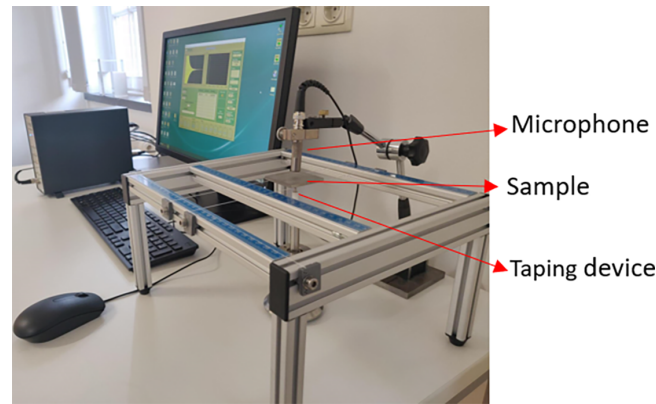


FIGURE 4 Resonant frequency method (RFM) test equipment.

3 | RESULTS AND DISCUSSIONS

3.1 | Density measurements and micrography

The density of Wrought 316 L stainless steel and samples printed with different parameters with LPBF in different sets, labeled A, B, C, and D as shown in Table 5. In terms of density, wrought 316 L has the highest value at 7990 Kg/m^3 , while LPBF Set-B exhibits the lowest density at 7913 Kg/m^3 . This comparison reveals variations in density introduced by the LPBF process, with each set showing nuanced differences in material properties. The changes observed underscore the impact of manufacturing methods on the mechanical characteristics of 316 L stainless steel.

Figure 5 shows the optical micrographs of four sets considered for this study, along with their planar views in each case. All the micro-graphs were obtained at $100 \mu\text{m}$ resolution. The melt pools are clearly visible in all the four sets in -ZX and -YZ plane. The parameter change didn't have an influence on the width of a single melt pool which was approximately $100 \mu\text{m}$. Whereas the effect on scan track can be seen in set-c, where (in -XY plane) the average width of the scan track is higher than other sets. The layers are apparent in the micrographs along the build direction, which depict a structure resembling layer. Figure 5E illustrates how these microstructures differ from a conventional austenitic structure. As is common with rolled and annealed austenitic sheets, the grain structure is equiaxed and contains twins in this instance. Stem crystals are produced by epitaxial crystal formation and grow polyhedrically outside of the layered structure. There, the elongated grains in the LPBF samples favor directional material features, which in turn favor anisotropy.⁵

3.2 | Comparison of frequencies from FEM and experiments for wrought samples

Based on the methodology elaborated in Section 2.3, the modal shapes along with the frequencies are elaborated in Figure 6. There are 10 modal frequencies shown in the figure below, the maximum at 35 kHz, and all the mode shapes are dominated by a mix of various flexure. The modes area combination of mode-1, mode-2, mode-3 and so forth according to an ascending order seen usually in geometrically mean part.¹⁸ The modal frequencies vary in a mode-specific way as a function of mechanical part structures. The modes seen below was obtained after performing a parametric study, wherein the frequency shift was ascertained by keeping the geometry fixed (the dimensions are same as the one used in experiments), while E-modulus is varied between a range of 180–200 GPa. It was observed that at 193 GPa, the frequency difference between the experiments and simulations narrowed down. From Table 4, the wrought 316 L material was seen to have an E-modulus of 190 GPa. This information helps in identifying the correct frequency from the experiments and canceling out others seen in the spectrum. The parametric study enables in identifying mode-1 frequency (7294 Hz) within the spectrum (which will be detailed in next sections), thus enabling one to identify the frequencies that one intends to identify in a spectrum while performing resonant frequency tests. It should be stated here that, since 10 reference samples were used to make the database of frequencies, simulated frequencies for each of those 10 samples (dimensions same as those in experiments) where obtained and was cross-checked to avoid any un-certainties.

TABLE 5 Evolution of density and E-modulus.

Sample	Density (Kg/m ³)
Wrought 316 L	7990
LPBF	
Set-A	7920
Set-B	7913
Set-C	7938
Set-D	7923

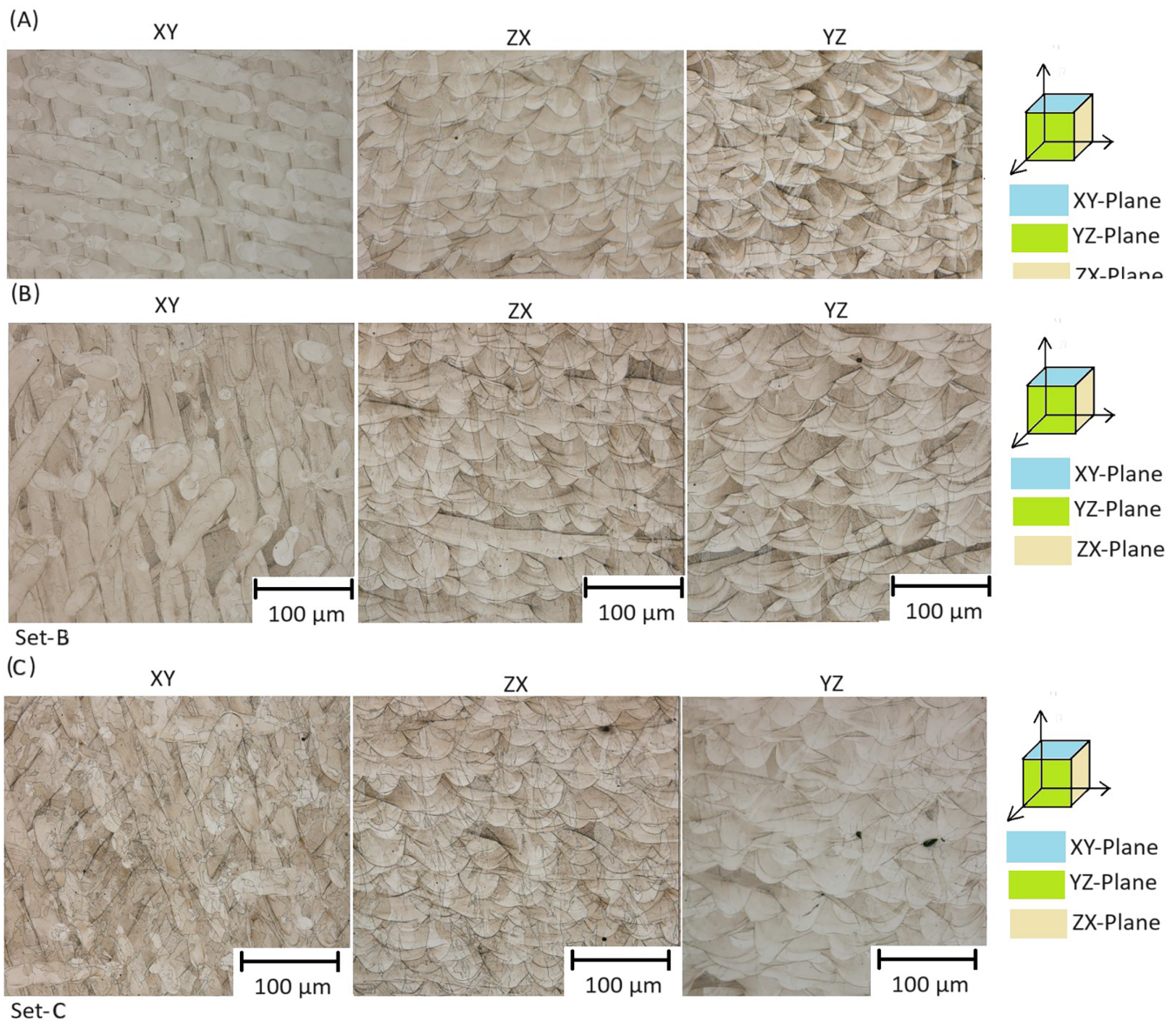


FIGURE 5 Microscopic images of LPBF Samples Set A, Set B, Set C, and Set D along with wrought samples.

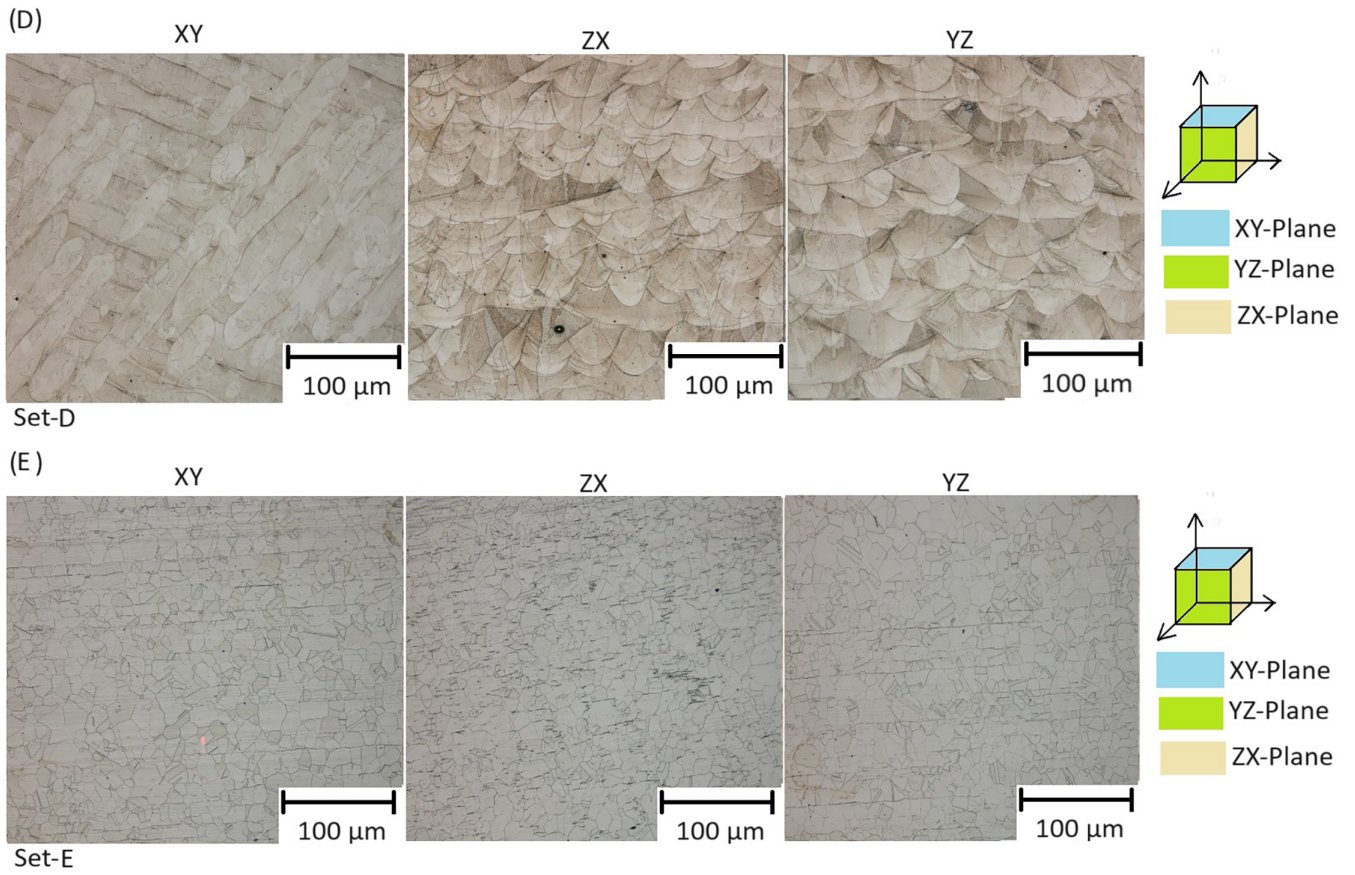


FIGURE 5 (Continued)

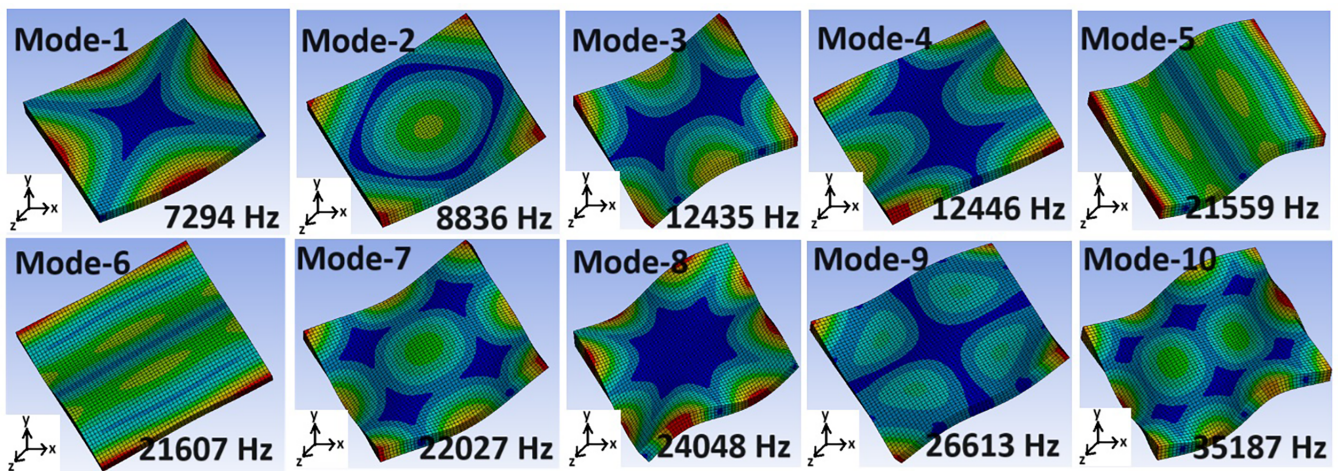


FIGURE 6 FEM calculated reference sample frequencies.

3.3 | Experimental signal acquisition, a routine for time-to-frequency domain conversion, and a methodology to classify samples based on quality

A typical time domain signal analysis is not ideal here because of its transient nature and hence is difficult to interpret the change and its cause. Therefore, we implement a frequency domain analysis in this paper, which requires a sub-algorithm, and such an algorithm would perform a time-to-frequency domain conversion. The time-to-frequency domain conversion can be performed via FFT (Fast Fourier Transforms), and here the sampling factor is an important factor. The sampling factor in the case of this paper was 200 kHz. The details of FFT can be found elsewhere and is beyond the scope of this paper. But the algorithm to realize the same shall be explained here and is shown pictorially in Figure 7. This algorithm shall be incorporated into the final sorting algorithm to classify samples.

First, the time signal is read, following which algorithm converts the same into frequency domain. There are several packages available within python, a few examples being NumPy, SciPy²⁷ and so forth. The steps are elaborated in flow chart in Figure 7, the time domain signal from 10 reference samples were fed into the algorithm. The frequencies were ascertained, and as seen in Figure 7, they remained between 7280 and 7320 Hz, the variation of the frequencies is related to the individual sample dimensions. This variation of approx. A total of 10 Hz was observed for a dimensional tolerance of ± 0.05 mm for all the reference sample studied in this paper. Thus, the frequency range of 7280–7320 Hz shall be fixed as an ideal range for reference, that is, a good sample shall have a frequency close to this range, provided the geometry remains within given tolerances. When cross-checked with the frequency for mode-1 in Figure 6, it remained within the range found here. The further the frequency moves away from this range toward left of the spectrum, the worst the samples are in terms of quality, with the condition that the geometry remains fixed.

Thus, based on this methodology, the Figure 8 was generated, where there are four spectrums from top to bottom. As the spectrum shifts from top to bottom, a given set of frequency range moves from left to right. In each of the spectrum, the peaks belong to a single sample from the respective lot, that is, for the spectrum at the top, each of the peaks belongs to each of the sample from set-B (10 Hz difference due to ± 0.05 dimensional tolerances). Therefore, set-B was seen to be the farthest from Reference (Ref in picture), whereas set-C was seen to be closest. Based on the methodology established to classify good sample in this paper, the closer the frequency is to the reference the better the samples are, and the farthest it goes, the worst they are in terms of quality. It was stated in Section 2.1 that Set-A was printed with a set of parameters assumed to be ideal and hence Set-A was seen to be better when compared to -B, -C and -D. But when observed in Figure 8, Set-C was closest to the reference and hence stands to be better than other sets. Moving it closer to reference shall be an ideal scenario, but it is difficult, since the maximum density achieved in the best sample set hasn't exceeded

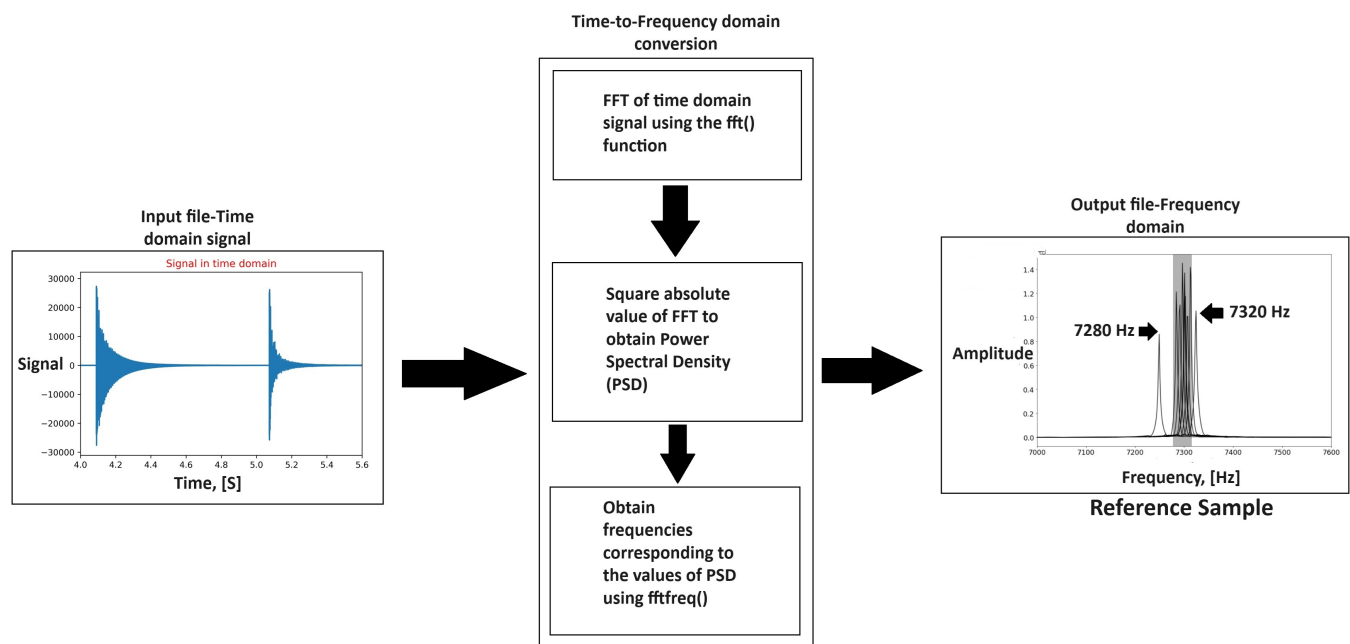


FIGURE 7 A sub-algorithm to convert a time-domain signal to a frequency-domain.

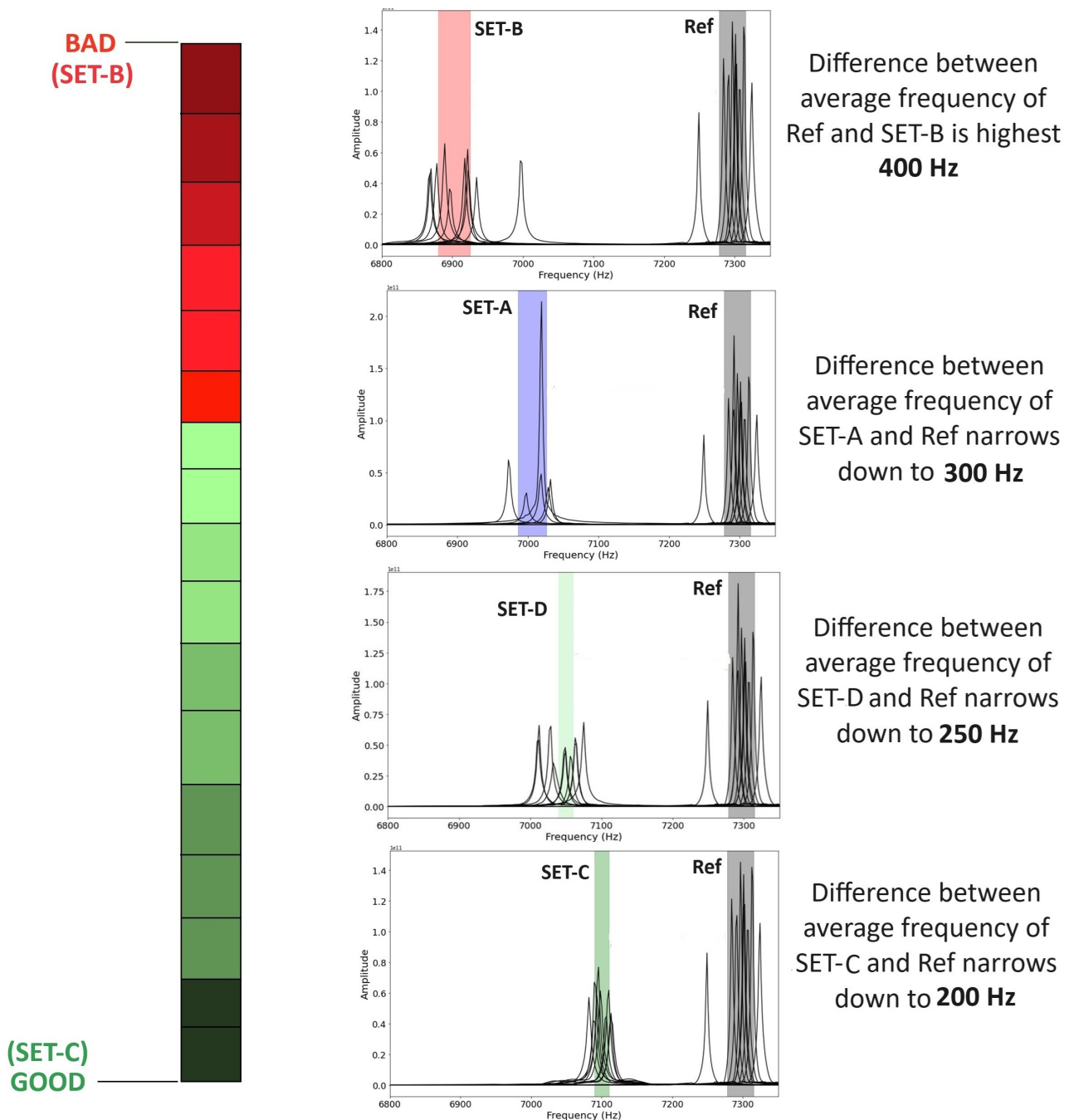


FIGURE 8 Frequency shifts seen on LPBF sample compared to the reference (Ref).

99.96% when compared to reference 35. In present study all samples were tested in as-built condition, set-C was seen to be 99.34% dense, which was higher when, compared set-B, which stood at 99.03%. Since all the samples were tested in as-built conditions, surface coarseness shall be an important aspect that might affect the frequency shifts. But surface treatments requires giving additional tolerances to the samples so that can be grinded or milled to the required precision. But this was avoided in this study since, surface treatments can introduce other distortions into the surface grain structure and the resulting frequency shifts could be attributed to these in addition to the density variation. Therefore, to minimize various un-certainties that affects frequency, samples were printed and cut to precise dimensions while the surface was untreated but having uniform thickness all over.

To further verify the methodology, a microscopic inspection of each sample from set -A, -B, -C, and -D was carried out (Figure 9). The porosity in different planes of each sample has been analyzed and evaluated. Microscopic investigation

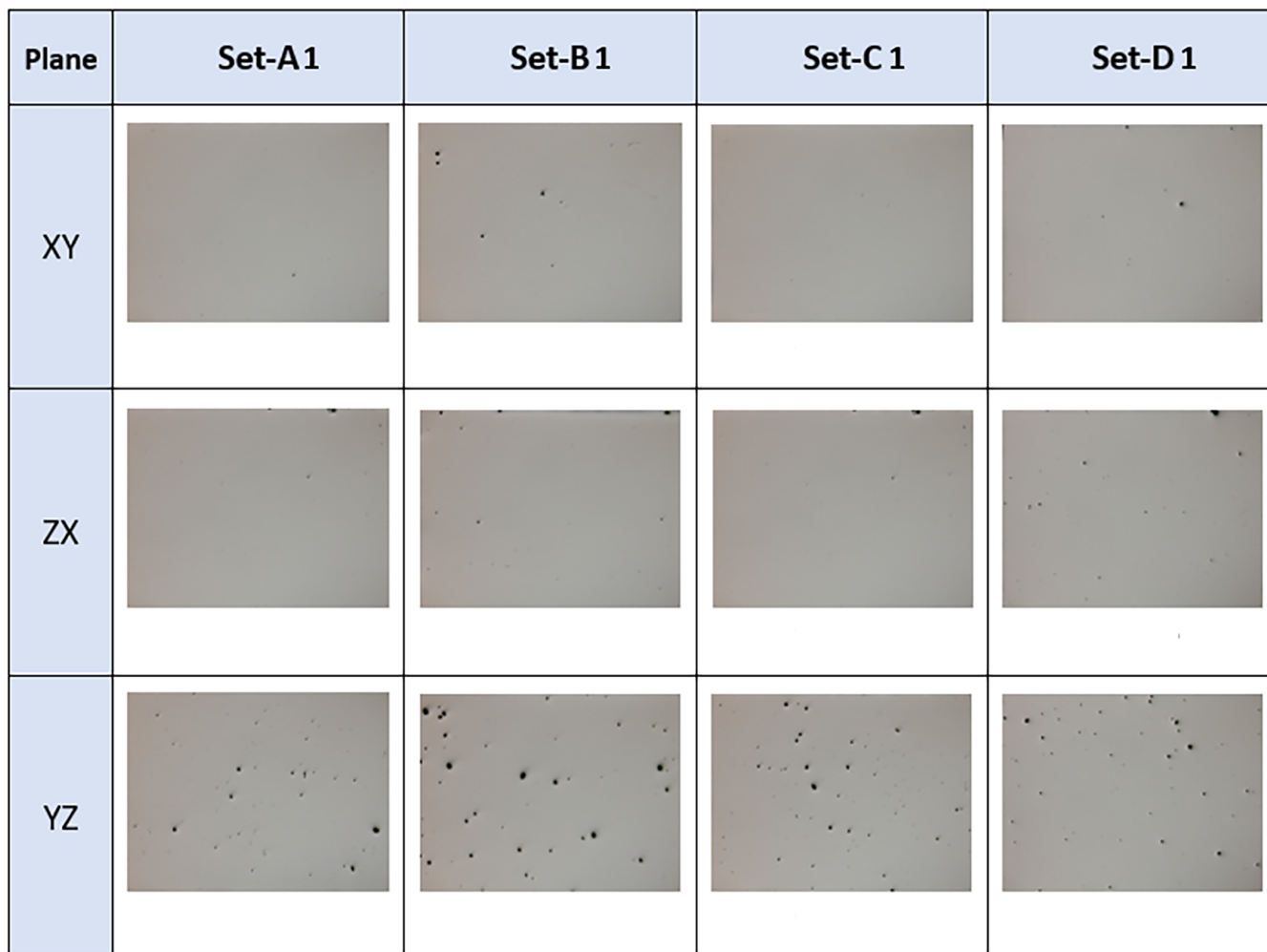


FIGURE 9 Porosity evaluation of LPBF sample under optical microscope (resolution 200 μm). A1, B1, C1, and D1 refers to sample no. 1 from the respective sample sets.

revealed a planar dependency for irregularities in printed samples. As an example, Figure 9 shows the planar dependency for porosity for different samples out of each set. Sample C1 from set-C was seen to have least porosity in planes -XY and -ZX, whereas some amount was in -YZ plane. B1 from sample set-B was seen to have a large concentration of porosity in its -YZ plane, followed by D1 and A1. To further quantify the observations, the porosity was calculated in terms of percentage in each plane and is depicted in Table 6.

Table 6 shows the maximum, minimum, and average porosity values for each of the three samples (-A, -B, -C, and -D) in the corresponding planes. Consistent with the findings in the preceding paragraph, samples from set-C exhibited the least porosity. A closer look at the table shows that all the sample had a high concentration of porosity in the -YZ plane. However, samples from set-C showed the least amount of variation within this plane. Unlike -YZ plane, -XY had the least concentration of porosity and here, samples from set-C had the least concentration. When this result is compared with density, set-C was the densest of all the sets considered, while set-B the least dense. Set-B being least dense is obvious as the sample sets from this group had the highest concentration of porosity in all the planes observed. When these observations are compared with Figure 8, where set-B was the farthest from reference while set-C the closest reveals the advantage of adopting such a methodology to qualify LPBF samples.

3.4 | An algorithmic approach to qualify samples based on print parameters

The algorithmic approach involves setting a minimum frequency difference between the average of reference samples so as to classify or assign them a class based on their quality. The definition of such classes of samples based on the difference

TABLE 6 Porosity in [%] in each plane of samples from Sets-A, -B, -C, and -D.

		Porosity %								
		Plane-XY			Plane-ZX			Plane-YZ		
		Max	Min	Mean	Max	Min	Mean	Max	Min	Mean
Set- A	1	0.09	0.08	0.08	0.14	0.10	0.12	0.41	0.36	0.39
	2	0.09	0.06	0.07	0.15	0.11	0.13	0.38	0.32	0.35
	3	0.09	0.07	0.08	0.15	0.10	0.13	0.45	0.39	0.42
Set- B	1	0.08	0.06	0.07	0.13	0.12	0.13	0.70	0.50	0.6
	2	0.07	0.05	0.06	0.15	0.11	0.13	0.65	0.53	0.59
	3	0.09	0.07	0.08	0.15	0.09	0.12	0.75	0.49	0.62
Set- C	1	0.05	0.03	0.04	0.08	0.06	0.07	0.31	0.22	0.27
	2	0.07	0.03	0.05	0.07	0.05	0.06	0.34	0.27	0.31
	3	0.06	0.02	0.04	0.09	0.07	0.08	0.35	0.29	0.32
Set- D	1	0.1	0.08	0.09	0.14	0.10	0.12	0.35	0.31	0.33
	2	0.09	0.06	0.07	0.15	0.11	0.13	0.36	0.32	0.34
	3	0.09	0.07	0.08	0.15	0.10	0.13	0.38	0.32	0.35

TABLE 7 Frequency range for quality classification.

Class	Difference between reference [Hz]
1-Best	<200
2-Good	>200 and <300
3-Average	>300 and <400
4-Worst	>400

in frequencies with reference is shown in Table 7. From Section 3.3 and Figure 9, the average frequency is 7300 Hz. Therefore, four classes of samples are defined, where Class-1 is the best, and in descending order of quality, Class-2 is good, Class-3 is average, and Class-4 is the worst. Based on such division, the algorithm is designed in such a way, that detected frequency above 7300 Hz (for constant sample dimensions) will be defined as the new reference frequency in the database and hence re-calculate the new frequency range for all the classes.

The algorithm based on the ranges elaborated previously is implemented and can be seen in Figure 10. Were the four classes of classification of samples are implemented along with an added ability of the algorithm to enlarge the database on which it relies to have a reference to all frequencies from the reference samples. Lastly, to validate the ability of the algorithm to detect, four additional samples were printed to check the frequency and classify them for its quality. The sample for the sake of convenience are termed as S1, S2, S3, and S4. S1 and S2 were printed based on parameters used to print Set-C, whereas S3 and S4 were printed with a laser power of 170 W and the rest of the parameters same as that of Set-C. Samples were precision milled to the dimensions used in this study and subsequently subjected to resonant frequency test to obtain the time-domain signals.

After subjecting S1, S2, S3, and S4, to the algorithm, it was classed into the first three classes of “Best,” “Good,” and “Average” (Table 8). Practically, S1 and S2 should have been classed into the “Best” category, but S2 was seen to be put in category “Good”. One reason could be that of internal porosity due to lack of fusion or pores with un-melted powder in it, since the dimensions were cross-checked with that of set-C. The tolerance was of the order ± 0.03 mm and hence doesn't warrant a drastic change in frequency seen between S1 and S2. A similar explanation holds true for S3 and S4. But it can be stated that the parameters used for set-C was found to be good in terms of reduced porosity and hence, the algorithm hasn't erroneously classed S1, S2 into other categories. In such a manner, the algorithm can be trained for a variety of geometries, by creating a database, which the algorithm can refer to and write into to be intelligent enough to class samples based on their frequencies. None of the sample could be classed in bad.

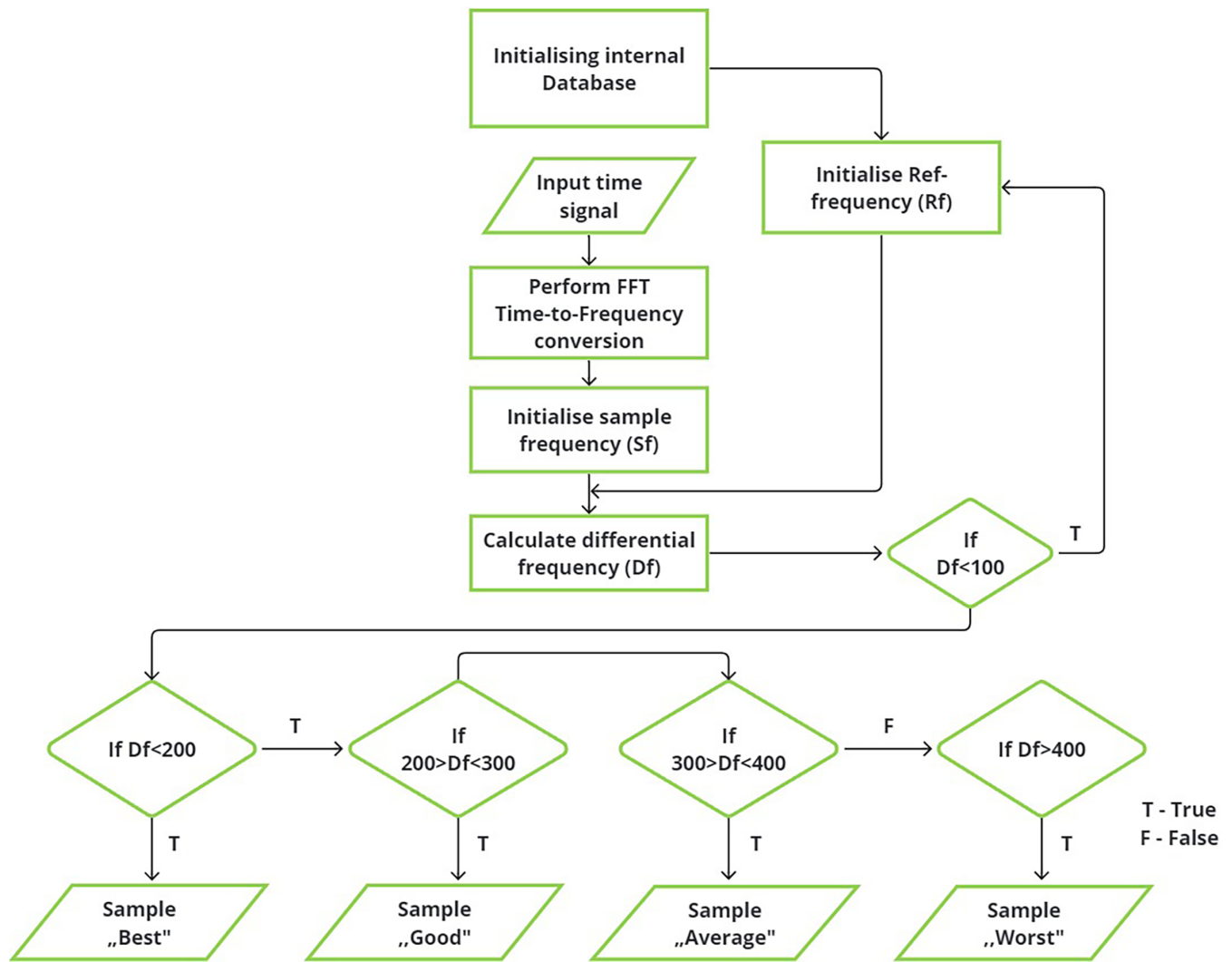


FIGURE 10 The sorting algorithm to classify LPBF samples based on their quality.

TABLE 8 Sample classification based on outcome from algorithm.

Sample No.	Class			
	1	2	3	4
S1	7128			
S2		7057		
S3			6921	
S4		7095		

4 | CONCLUSION

The paper attempts to sort flawed LPBF samples printed from 316 L steel powder by comparing its natural frequency to wrought 316 L steel and hence a reference of a natural frequencies is generated. Initially, wrought 316 L samples were precision milled from its plate to a set dimension. It was subjected to RFM to ascertain its natural frequencies. Later, simulations were performed to obtain the natural frequencies, where the material properties were obtained through samples cut from the same plate from samples for RFM were milled. The geometry of the samples for simulations were the same

as those subjected to RFM, and the resulting simulated frequencies coincided. Thus, the reference based on which the quality of LPBF samples is established. Four set of LPBF samples were printed with different parameters and samples were milled to the same dimensions as that of the reference samples. All of them were subjected to RFM and through a sub-algorithm of the main sorting algorithm, the natural frequencies were recorded and compared with that of reference. The closer the frequencies are to the reference the better they are based on their density. Thus, Set-C samples were found to be close to the reference and to confirm their quality with respect to other sets, microscopic investigations were performed. It was observed that set-B had the highest porosity in all planes, whereas set-C had the least, this was confirmed with the density of the sample. Set-B was less dense among all the sets, while set-C had the highest. Based on this inference, an algorithm to sort LPBF sample was implemented, and the fundamental sorting criteria was fixed on the frequency difference between the LPBF samples and the reference. Any frequency difference between LPBF and the reference less than 200 Hz was classed as best and the difference if exceed 400 Hz was classed as worst. The algorithm was checked for its efficacy on four new samples printed for this purpose and it was found to sort them satisfactorily. The algorithm can be made more versatile by making it to learn more data on samples with different sizes and hence an effective algorithm for quality assessment can be realized. Such a routine can finally be implemented on a hardware that can effectively help in quality assurance and help to establish AM as an effective and efficient alternative to conventional manufacturing processes.

AUTHOR CONTRIBUTIONS

Suresh Alaparthi: Investigation; validation; software; formal analysis; data curation; writing – original draft. **Sharath P. Subadra:** Conceptualization; writing – original draft; methodology; validation; visualization; writing – review and editing; data curation. **Roy Skaria:** Software; writing – original draft. **Eduard Mayer:** Project administration; data curation. **Shahram Sheikhi:** Conceptualization; funding acquisition; methodology; project administration; writing – review and editing; resources; supervision; validation.

ACKNOWLEDGMENTS

1. This is a part of research project “3DPrintFEM” along with cooperation partner Werkstoffprüfung Kunze GmbH. This project has received funding from the Bundesministerium für Wirtschaft und Klimaschutz (BMWK) Zentrales Innovationsprogramm Mittelstand (ZIM).
Link: <https://www.haw-hamburg.de/forschung/forschungsprojekte-detail/project/project/show/3dprintfem/>
2. Werkstoffprüfung Kunze GmbH (Hagen, Germany) for all the materials.
3. Ms. Vera Liedtke-Scheffler, University of Applied Science Hamburg, Institute of Materials Science and Joining Technology, Berliner Tor 13, D-20099, Germany.
4. We acknowledge support for the article processing charge by the programme “Open Access Publication Costs/2024–2026/Hamburg University of Applied Sciences” funded by the Deutsche Forschungsgemeinschaft (DFG)–Project number 532170006.

Open Access funding enabled and organized by Projekt DEAL.

CONFLICT OF INTEREST STATEMENT

The authors declare no conflicts of interest.

PEER REVIEW

The peer review history for this article is available at <https://www.webofscience.com/api/gateway/wos/peer-review/10.1002/eng2.12996>.

DATA AVAILABILITY STATEMENT

The data that support the findings of this study are available on request from the corresponding author. The data are not publicly available due to privacy or ethical restrictions.

ORCID

Sharath P. Subadra  <https://orcid.org/0000-0002-7558-638X>

REFERENCES

1. Vafadar A, Guzzomi A, Rassau A, Hayward K. Advances in metal additive manufacturing: a review of common processes, industrial applications, and current challenges. *Appl Sci*. 2021;11(3):1213.
2. ASTM I. *Standard Terminology for Additive Manufacturing Technologies (F2792-12a)*. ASTM; 2009.
3. Uhlmann E, Kersting R, Klein TB, Cruz MF. Wire-based laser metal deposition for additive manufacturing of TiAl6V4: basic investigations of microstructure and mechanical properties for buildup parts. *Procedia CIRP*. 2015;35:55-60.
4. Wang P, Li HC, Prashanth KG, Eckert J, Scudino S. Selective laser melting of Al-Zn-Mg-Cu: heat treatment, microstructure, and mechanical properties. *J Alloy Compd*. 2017;707:287-290.
5. DebRoy T, Wei HL, Zuback JS, et al. Additive manufacturing of metallic components – process, structure and properties. *Prog Mater Sci*. 2018;92:112-224.
6. Zhou C, Wu F, Tang D, Zhang Z, Zhang L, Zheng J. Effect of subcritical-temperature heat treatment on corrosion of SLM SS316L with different process parameters. *Corros Sci*. 2023;218:111214.
7. Liverani E, Toschi S, Ceschini L, Fortunato A. Effect of selective laser melting (SLM) process parameters on microstructure and mechanical properties of 316L austenitic stainless steel. *J Mat Process Tech*. 2017;249:255-263.
8. Nandhakumar R, Venkatesan K. A process parameters review on selective laser melting-based additive manufacturing of single and multi-material: microstructure, physical properties, tribological, and surface roughness. *Mater Today Commun*. 2023;35:105538.
9. Zhang B, Li Y, Bai Q. Defect formation mechanisms in selective laser melting: a review. *Chin J Mech Eng*. 2017;30(3):515-527.
10. Jia H, Sun H, Wang H, Wu Y. Scanning strategy in selective laser melting (SLM): a review. *Int J Adv Manuf Technol*. 2021;113:2413-2435.
11. Caiazzo F. Additive manufacturing by means of laser-aided directed metal deposition of titanium wire. *Int J Adv Manuf Technol*. 2018;96:2699-2707.
12. Taghipour A, Mazaheri Y, McDavid J, et al. Strengthening mechanisms and strain hardening behaviour of 316L stainless steel manufactured by laser-based powder bed fusion. *Adv Eng Mater*. 2023;25:2201230.
13. Gorsse S, Hutchinson C, Gouné M, Banerjee R. Additive manufacturing of metals: a brief review of the characteristic microstructure and properties of steels, Ti-6Al-4V and high-entropy alloys. *Sci Technol Adv Mater*. 2017;18:584-610.
14. Lu Y, Zhu Z, Yin A, et al. Evaluation of corrosion resistance of 316L stainless steel by laser ultrasonic nondestructive testing technology. *Mater Res Express*. 2023;10(9):096519.
15. Seifi M, Salem A, Beuth J, Harryson O, Lewandowski JJ. Overview of materials qualification needs for metal additive manufacturing. *JOM*. 2016;68(3):747-764.
16. Rossin J, Goodlet B, Torbet C, et al. Assessment of grain structure evolution with resonant ultrasound spectroscopy in additively manufactured nickel alloys. *Mater Character*. 2020;167:110501.
17. du Plessis A, Yadroitsev I, Yadroisteva I, Le Roux SG. X-ray microcomputed tomography in additive manufacturing: a review of the current technology and applications. *3D Print Additiv Manuf*. 2018;5(3):227-247.
18. Heinrich M, Valeske B, Rabe U. Efficient detection of defective parts with acoustic resonance testing using synthetic training data. *Appl Sci*. 2022;12(15):7648.
19. Alaparthi S, Subadra SP, Sheikhi S. A smart, data-driven approach to qualify additively manufactured steel samples for print-parameter-based imperfections. *Materials*. 2024;17(11):2513.
20. Lee Y, Chung M. A study on crack detection using eigenfrequency test data. *Comput Sci*. 2000;77:327-342.
21. Kam TY, Lee TY. Detection of cracks in structures using modal test data. *Eng Fract Mech*. 1992;42:381-387.
22. West BM, Capps NE, Urban JS, et al. Modal analysis of metal additive manufactured parts. *Manufact Lett*. 2017;13:30-33.
23. Urban J, Capps N, West B, et al. *Towards Defect Detection in Metal SLM Parts Using Modal Analysis 'Fingerprinting'*. Solid Freeform Fabrication Symposium; 2017.
24. Belyaev A, Polupan O, Ostapenko S, Hess D, Kalejs JP. Resonance ultrasonic vibration diagnostics of elastic stress in full-size silicon wafers. *Semiconductor Sci Technol*. 2006;21:254-260.
25. Dallas W, Polupan O, Ostapenko S. Resonance ultrasonic vibrations for crack detection in photovoltaic silicon wafers. *Measure Sci Technol*. 2007;18:852-858.
26. Greco S, Gutzeit K, Hotz H, et al. Selective laser melting (SLM) of AISI 316L-impact of laser power, layer thickness, and hatch spacing on roughness, density, and microhardness at constant input energy density. *Int Adv Manuf Technol*. 2020;108:1551-1562.
27. Virtanen P, Gommers R, Oliphant TE, et al. SciPy 1.0: fundamental algorithms for scientific computing in python. *Nature Methods*. 2020;17:261-272.
28. Pisarciuc C, Dan I, Cioară. The influence of mesh density on the results obtained by finite element analysis of complex bodies. *Materials*. 2023;16(17):2555.
29. Sufiiarov VS, Popovich AA, Borisov EV, et al. The effect of layer thickness at selective laser melting. *Procedia Eng*. 2017;174:126-134.
30. DIN EN 843-2. Hochleistungskeramik-Mechanische Eigenschaften monolithischer Keramik bei Raumtemperatur-Teil2: Bestimmung des Elastizitätsmoduls, Schubmoduls und der Poissonzahl. *Deutsche Fassung*. 2007.
31. Lewandowski JJ, Seifi M. Metal additive manufacturing: a review of mechanical properties. *Annu Rev Mat Res*. 2016;46:151-186.
32. DIN EN ISO/ASTM 52900:2022-03. *Additive Fertigung-Grundlagen-Terminologie/additive manufacturing-Generl principles-fundamentals and vocabulary*. ISO/ASTM. 2002.
33. Keller T, Lindwall G, Ghosh S, et al. Application of finite element, phase-field, and calphad-based methods to additive manufacturing of ni-based superalloys. *Acta Mater*. 2017;139:244-253.

34. Collins PC, Brice DA, Samimi P, Ghamarian I, Fraser HL. Microstructural control of additively manufactured metallic materials. *Annu Rev Mat Res*. 2016;46:63-91.
35. Mustafa AWD, Siddique S, Johannsen J, et al. *Quality assurance of additively manufactured alloys for aerospace industry by non-destructive testing and numerical modelling*. 10th International Symposium on NDT in Aerospace. 2018. <https://www.ndt.net/article/aero2018/papers/Th.4.A.1.pdf>

How to cite this article: Alaparthy S, Subadra SP, Skaria R, Mayer E, Sheikhi S. A study on the effect of print parameters on the internal structural quality of 316 L samples printed via laser powder bed fusion: Experimental and algorithmic approach. *Engineering Reports*. 2024;e12996. doi: 10.1002/eng2.12996